
3D bulk measurements of the force distribution in a compressed emulsion system

Jasna Brujić,^a Sam F. Edwards,^a Dmitri V. Grinev,^a Ian Hopkinson,^{†a}
Djordje Brujić^b and Hernán A. Makse^c

^a *Polymers and Colloids Group, Cavendish Laboratory, University of Cambridge, Madingley Road, Cambridge, UK CB3 0HE*

^b *Imperial College of Science Technology and Medicine, Exhibition Road, London, UK SW7 2AZ*

^c *Levich Institute and Physics Department, City College of New York, New York NY 10031, US*

Received 8th May 2002, Accepted 13th June 2002

First published as an Advance Article on the web 3rd October 2002

In particulate materials, such as emulsions and granular media, a “jammed” system results if particles are packed together so that all particles are touching their neighbours, provided the density is sufficiently high. This paper studies through experiment, theory and simulation, the forces that particles exert upon one another in such a jammed state. Confocal microscopy of a compressed polydisperse emulsion provides a direct 3D measurement of the dispersed phase morphology within the bulk of the sample. This allows the determination of the probability distribution of interdroplet forces, $P(f)$ where f is the magnitude of the force, from local droplet deformations. In parallel, the simplest form of the Boltzmann equation for the probability of force distributions predicts $P(f)$ to be of the form $e^{-f/p}$, where p is proportional to the mean force \bar{f} for large forces. This result is in good agreement with experimental and simulated data.

1 Introduction

The concept of jamming is emerging as a fundamental feature of many systems with slow relaxation dynamics such as granular matter, complex fluids and structural glasses.^{1,2} Whereas one can think of liquids or suspensions as consisting of particles which move very slowly compared to gases, there comes a point where all particles are in close contact with one another and therefore experience structural arrest. In granular systems and compressed emulsions there is no kinetic energy of consequence; the typical energy required to change the positions of the jammed particles is very large compared to the thermal energy at room temperature. As a result, the material remains arrested in a metastable state and is able to withstand an applied stress.³

There is a growing literature studying the “jammed” state in particulate assemblies, aiming to characterise its micromechanics.¹ It has been shown experimentally that the stresses are distributed inhomogeneously through granular materials and the features of the distribution are useful in

[†] Department of Physics, UMIST, Sackville Street, Manchester, UK M60 1QD.

inferring the structural elements associated with mechanisms of supporting the applied stress. In order to develop a theory to describe such closely packed particles one needs to know the geometry of the packing in the bulk, and the distribution and propagation of stress in these systems.

Several approaches have so far been employed, including 2D and 3D experimentation,^{4,5} numerical simulations^{6–10} and statistical modelling.¹¹ Previous experiments in 3D assemblies have been confined to measurements of the probability distribution of forces exerted at the boundaries with the container, thus reducing the dimensionality of the problem.^{5,8,12–14} These measurements provide a quantitative understanding of the inhomogeneity of stress transmission within the bulk. However, the method does not have access to the spatial arrangement of the contact force network and other structural features, such as force chains and arching, which have been postulated as the signature of jamming.^{1,10}

The salient feature of the probability distribution $P(f)$ of interparticle contact force f in jammed systems, obtained from the above methods, is an exponential decay above the mean value of the force. This feature of $P(f)$ seems very robust, with growing evidence that it is independent of particle rigidity,^{6,9} crystallinity,¹⁴ tangential forces, construction history and friction.⁸ Nevertheless, there is no clear consensus on the general functional form of $P(f)$ as there are significant discrepancies in the literature particularly regarding the behaviour at small forces, both between experimental data and the theoretical model predictions. Moreover, the possibility of a crossover to a Gaussian-like distribution has been observed at large confining pressures.^{7,8,15}

In this paper we present a novel method to measure the force distribution within a concentrated emulsion system in its jammed state, which provides the complete three-dimensional information of the contact force network and the spatial arrangement of droplets. We address this problem using confocal microscopy, which provides direct measurement of the dispersed phase morphology within the bulk of the sample. The emulsion droplets are compressed by an external pressure through centrifugation because of the density difference between the phases, and a force network develops within the system in response to the applied stress. At high volume fractions, above the random close packing regime, emulsions exhibit an elasticity which is rationalised by the storage of energy through the deformation of droplets, given in terms of their Laplace pressure.¹⁶ The degree of deformation is used to derive an interdroplet force. The 3D imaging of a whole ensemble allows the calculation of the forces between the droplets, thus enabling the determination of $P(f)$. We find that the distribution is characterised by a small peak at low forces and an exponential decay at forces above the mean value, a result that can be described by the functional form of $P(f)$ derived from the simple theoretical model we propose in this paper.

The form of the probability distribution is independent of the material of the particle provided it has well defined elastic properties. Therefore we can expect the micromechanics of an emulsion, comprised of very “soft” particles, to bear many similarities with a packing of granular materials, such as ball bearings or glass beads. Even though there have been no studies of $P(f)$ specifically devised for compressed emulsion systems, we compare our results with the existing data for other jammed systems such as grains and foams, thus testing the hypothesis of a common behaviour for all such matter.

We use numerical simulations to examine the effect of polydispersity, osmotic pressure, and other microstructural features, such as the coordination number, on the distribution of forces. They are designed to mimic the experimental procedure on monodisperse and polydisperse distributions of soft particles. The numerical simulation result at the appropriate confining pressure is in good agreement with that obtained from the experiment, showing that the form of the force distribution is indeed independent of particle polydispersity.

Moreover, we offer in this paper what we believe is the simplest realistic theory of the force distribution, a theory which does not attempt the ambitious study of the percolation of forces,¹⁷ but has the advantage of a simple analytic solution. The theory is sufficiently crude that the reader will be able to see all sorts of ways in which it can be improved, however the simple prediction of the theory can easily be compared to experimental results and is found to describe the data well.

2 Experiment

Confocal microscopy is an optical microscopy whose key feature is that only light from the focal plane is detected. Thus 3D images of translucent samples can be acquired by moving the sample

through the focal plane of the objective and acquiring a sequence of 2D images. The spatial resolution of this technique is of order $0.5\ \mu\text{m}$ and the temporal resolution depends on the detail of the microscope used. Confocal microscopy is widely used in the biological sciences, but is now seeing application to a wide range of problems in soft matter physics, including colloidal crystallization,^{18,19} glassy dynamics,²⁰ 3D director orientation,²¹ determination of the geometry of a particle ensemble²² and interfacial structures in phase separated systems.²³

We use a Zeiss LSM510 confocal laser scanning microscope equipped with a high numerical aperture oil-immersion objective lens with a $40\times$ magnification. The fluorescent dye is excited with a 488 nm Argon laser and the emitted light is detected using a photomultiplier behind a long-pass 505 nm filter. These settings are appropriate for the excitation of Nile Red dye, used to label the emulsion described in more detail below. The sample volume ($76.3 \times 76.3 \times 23.6\ \mu\text{m}$) is typically acquired from regions $30\ \mu\text{m}$ below the upper surface of the sample. In this work a 3D image is acquired in approximately 2 min.

The emulsion system constitutes of silicone oil droplets in a refractive index matching solution of water ($w_t = 50\%$) and glycerol ($w_t = 50\%$), stabilised by 0.01 mM sodium dodecylsulfate (SDS). This system is a modification of the emulsion reported by Mason *et al.*²⁴ to produce a transparent sample suitable for confocal microscopy. Preliminary experiments showed that a very good refractive index match (0.02 units) between the continuous and dispersed phase of the emulsion is required in order to allow the acquisition of high quality images. Micropipette additions of the appropriate component of the water phase are therefore used to fine-tune the refractive index match after the initial emulsification. For a poorly matched high volume fraction, emulsion scattering at the interfaces leads to a rapid degradation of the image quality as a function of depth into the sample, as many interfaces are crossed. A further requirement is that the emulsion remains stable to coalescence and Ostwald ripening, which is not trivial in a system where the water phase has been modified to increase its refractive index.

The droplet size distribution, measured by image analysis, gives a mean radius of $3.4\ \mu\text{m}$ with a radius range between $1\ \mu\text{m}$ and $10\ \mu\text{m}$, shown in Fig. 1. This relatively narrow droplet size distribution is achieved by applying high shear rates ($7000\ \text{s}^{-1}$) to a coarsely mixed parent emulsion using a Linkam shear stage.²⁵ At this level of polydispersity crystallisation is avoided. To provide contrast between the phases in the microscope, the dispersed oil phase is fluorescently labelled by adding 0.1 mM solution of Nile Red dye, predissolved in acetone. The emulsion system prepared in this way remains stable to coalescence for at least six months.

The threshold volume fraction for the onset of elasticity depends on the polydispersity of the emulsion, or in other words, the efficiency of the packing. The sequence of images in Fig. 2 shows 2D slices from the middle of the sample volume after: (a) creaming under gravity, (b) centrifugation at $6000g$ for 20 min and (c) centrifugation at $8000g$ for 20 min. The samples were left to equilibrate for several hours prior to measurements being taken. Since jamming is accompanied by the appearance of flattened areas of contact between droplets and their deformation away from spherical, the volume fraction corresponding to a state near the “jamming” transition is easily

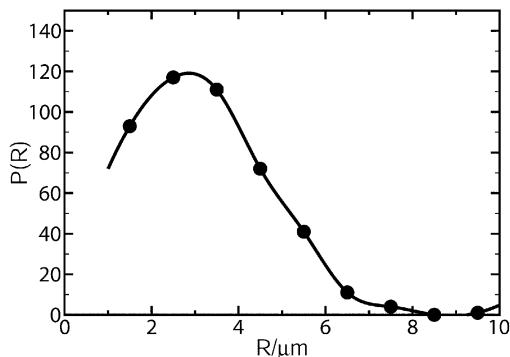


Fig. 1 Droplet size distribution.

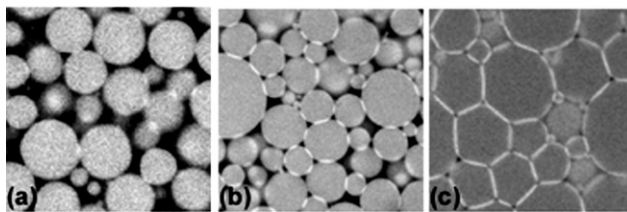


Fig. 2 2D slices of emulsions under varying compression rates: 1g (a), 6000g (b) and 8000g (c).

identified visually, as shown in Fig. 2(b). The volume fraction for our polydisperse system shown is $\phi = 0.90$, determined by image analysis. This high volume fraction obtained at a relatively small osmotic pressure of 125 Pa is achieved due to the polydispersity of the sample.

2.1 Image analysis

Confocal imaging of the static sample revealed an interesting physical effect which occurs upon emulsion compression. The areas of contact between the droplets fluoresce with a higher intensity than the undeformed perimeters on the bodies of the droplets, thus highlighting the regions of interest. Images presented in Fig. 2 clearly show a preferential diffusion of the dye into the surfaces of contact as the osmotic pressure is increased. This effect can be attributed to the increase in surfactant concentration at the regions of deformation as two droplet surfaces are pushed together. The fluorescent dye has an affinity for the surfactant so that an enhanced surfactant concentration leads to an enhanced dye concentration and thus higher fluorescence. Future work will involve a more thorough investigation of this effect.

We describe two schemes by which the forces between the droplets are calculated from the 3D images. The output for both of these methods is a set of contact areas, along with the undeformed radii of the two droplets giving rise to each contact. This data enables the extraction of the normal force by means of existing interdroplet force models, discussed in Section 2.2. The first stage for both methodologies is to extract the positions and radii of all the droplets with subvoxel accuracy. This task is not trivial given the polydispersity of particle sizes and their high packing fraction within the volume. One approach to this problem is to apply an intensity threshold, followed by morphological operations to separate the droplets which are left connected by the original threshold. We found that this method did not provide the required accuracy and was computationally very intensive for the large image volumes used in this experiment ($256 \times 256 \times 64$ voxels).

An alternative method to finding the emulsion droplets is to use the fact that they are spherical to a good approximation. We can consider the emulsion as a set of spheres of different sizes convolved with a set of delta functions. The convolution theorem of Fourier transforms thus gives us a route to finding spheres of a particular size. More generally, the Fourier transform converts spatial features into frequencies and provides a mathematical mechanism for building filters which remove or enhance features of a particular frequency domain in an image. The following relation describes the Fourier Filtering Method (FFM) applied to our problem.²⁶

$$F = I \times H + N \quad (1)$$

where F is the Fourier transform of the acquired 3D image, I is the Fourier transform of a perfect sphere of size R , H is the Fourier transform of the set of delta functions related to sphere positions and N is the noise. Assuming the noise is negligible compared to the other terms, it is possible to determine H from a simple algebraic manipulation: $H = F/I$. Ideally the inverse Fourier transform of the resultant array provides an image of delta functions marking the centres of spheres of size R .²⁷

However, the process is very susceptible to noise. We therefore apply the Wiener filter, designed to work in cases where the noise has become significant. An approximation of this filter can be expressed as follows:

$$H = \frac{F}{I} \times \frac{\|I\|^2}{\|I\|^2 + K} \quad (2)$$

where $\|J\|^2$ is the norm of the complex number J and K is a constant. The value of K in this case is the squared variance of the noise.

The process is then repeated for the appropriate range of radii with an increment of $0.1 \mu\text{m}$ to extract all the spheres in the original 3D image. The increment size corresponds to the limit of accuracy of this image analysis technique, *i.e.* $1/3$ of a pixel.

The resulting image of the inverse Fourier transform for a given value of R contains not only the centres of the particles with the correct radius (which appear as bright delta functions), but also those of incorrect radii, as well as considerable noise contributions from all other features in the original image which have not been eliminated by the Wiener filtration. Therefore the procedure to test the significance of a particular feature requires further selection. Firstly, for each value of R , all sphere contributions appear as bright voxel clusters and can be readily thresholded by intensity as being higher than half of the maximum intensity value in the image. The centre of each cluster is then determined as its centre of mass weighted by intensity and is the key feature in achieving subvoxel accuracy in the coordinates of the sphere centres. Secondly, if large intensities are observed in the same region of the sample volume for a number of different model values of R , it can be assumed that the significant feature really exists.²⁸ Only those intensities are accepted and the centre of the particle is taken to be the position of the maximum of all peaks found in the region. Given this filtering, we are able to obtain all sphere radii and positions within the body of the 3D volume. Spheres that cut the boundaries of the volume by more than half of their radius are not identified reliably and are therefore excluded from further analysis. The use of such a “guard” region is common practice in image analysis.

To measure the accuracy of the particle finding algorithm we apply the process to a synthetic dataset with known particle centers, radii and added noise. The algorithm is able to recover the size of these ‘synthetic’ spheres with an accuracy of around $1/3$ of a pixel and even higher accuracy is achieved in finding the positions of the sphere centres. Furthermore, the algorithm also finds particles cut by the boundaries of the volume, suggesting a degree of tolerance to particle deformation. An illustration of the accuracy in reconstructing the droplets is presented in Fig. 3. The obvious discrepancies between the two arise from more pronounced shape deformations of droplets in some cases and from the blurred contributions of features that are above or below the focal plane of interest. We find only a 2% lower volume fraction of the dispersed phase in the reconstruction when compared with the value obtained by a direct threshold of the original image, which is a good indication of the information lost by the analysis methodology.

In the second stage, once the particles have been found, two different methods are applied for isolating the areas of deformation, and therefore the forces. The first method measures the size of the contact areas between the reconstructed spheres by the application of simple geometric considerations, as shown in Fig. 4. It calculates the circular plane of intersection of the spheres in contact, from which we determine the force assuming a linear order in the deformation and ignoring the changes in droplet shape, discussed in Section 2.2.

In the second method, the contact patches shown in Fig. 2(b); are extracted based on an intensity threshold, since they are brighter than either the droplets or the aqueous background. In practice,

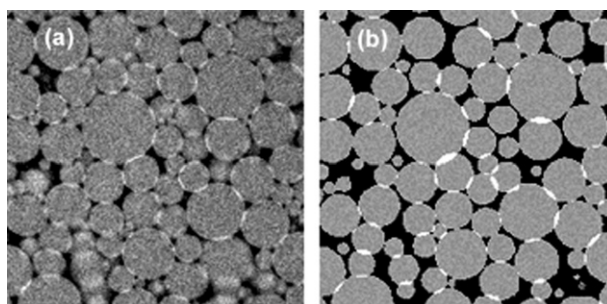


Fig. 3 Comparison of 2D images obtained from (a) acquired data and (b) reconstructed data using Fourier Filtering Method.

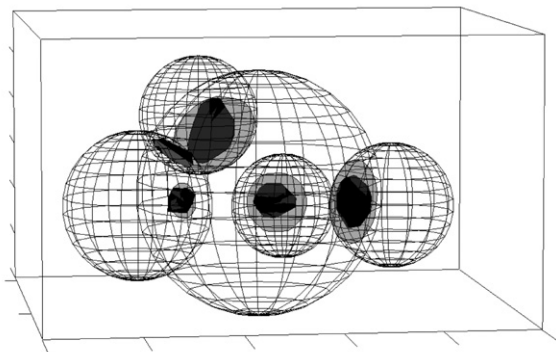


Fig. 4 Comparison between circular planes of intersection of the spheres in contact obtained from their geometric overlap and those from highlighted patches in the original images, from which we determine the force.

this is achieved by applying morphological operations on the binary image to remove isolated pixels and to bridge separated ones belonging to the same contact. All objects are then labelled and those below a threshold pixel density within the contact are eliminated due to their diffuse nature, often attributable to noise. The second filtration process sets a minimum area of the labelled contact ($1 \mu\text{m}^2$) in 3D to avoid noise contribution to the statistics at low forces. Thus, we set a limit to the lowest force we can detect in order to be sure of its accuracy. The areas of contact are overestimated because the original fluorescence gives the impression of volume elements between droplets, rather than contact planes. In order to “flatten” the contacts into circular patches we perform a method which firstly attributes each of the obtained contact regions to the corresponding two droplets giving rise to it. Furthermore, only the voxels from the region belonging to both droplets are selected to avoid the merging of different contact regions. In order to obtain flat surfaces of contact, these voxels are projected onto the plane normal to the line joining the corresponding droplet centres. The plane coincides with that obtained *via* the first geometric method of defining the overlap. The resultant area of the set of projected voxels is obtained from the polygon defined by their convex hull, calculated as the sum of the triangles that the polygon is divided into (Fig. 5). By contrast to the first method, these areas are calculated by measurement of an effect arising from real forces within the system, and hence take into account all non-linear effects in the droplet response to the applied stress.

2.2 The force model

While granular materials interact *via* normal and tangential forces (both contact and dissipative),⁸ other athermal soft matter systems such as emulsions²⁹ and foams³⁰ are considered to interact with only normal forces (repulsive and dissipative) at concentrations above the random close packing (RCP). The determination of an accurate force model for the compression of two droplets is not trivial, but can be simplified within certain limits. For small deformations with respect to the droplet surface area, the Laplace pressure remains unchanged and all the energy of the applied stress is presumed to be stored in the deformation of the surface. Hence, at the microscopic level, two spherical droplets in contact with radii R_1 and R_2 interact with a normal force

$$f = \frac{\sigma}{\bar{R}} A \quad (3)$$

This is the Princen model,¹⁶ where A is the area of deformation, σ is the interfacial tension of the droplets and \bar{R} is the geometric mean of the radii of the undeformed droplets, $\bar{R} = 2R_1R_2/(R_1 + R_2)$. The normal force acts only in compression, *i.e.* $f = 0$ when there is no overlap.

The above force corresponds to an energy of deformation which is quadratic in the area of deformation, analogous to a harmonic oscillator potential that describes a spring satisfying

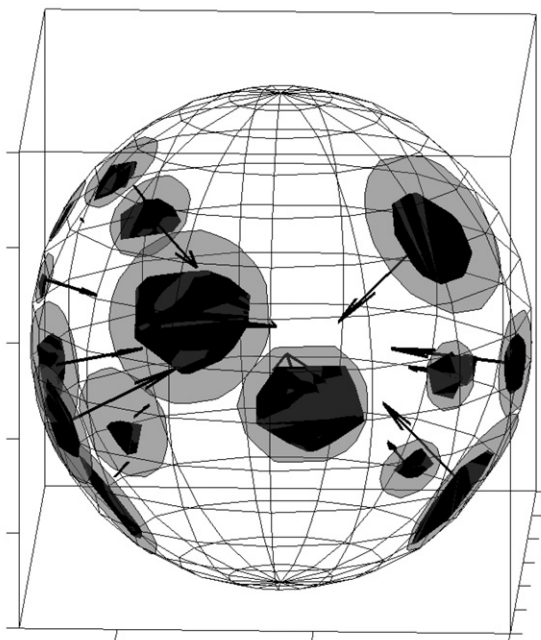


Fig. 5 All surfaces of contact and compression forces calculated from them for one sphere within the sample volume. Forces are shown as arrows of length proportional to their magnitude.

Hooke's law. There have been several more detailed calculations³¹ and numerical simulations²⁹ to improve on this model and allow for anharmonicity in the droplet response by also taking into consideration the number of contacts by which the droplet is confined. Typically these improved models lead to a force law for small deformations of the form $f \propto A^\alpha$, where α is a coordination number dependent exponent in the range 1–1.5.

In our experiment, the discrepancy of the areas observed as the highlighted regions of the images and those calculated from a geometric overlap which ignores the response of the droplet shape to the deformation and the number of surfaces the droplet is confined by, provides a direct measure of the effects of anharmonicity of the interaction between the droplet surfaces (Fig. 6). The areas

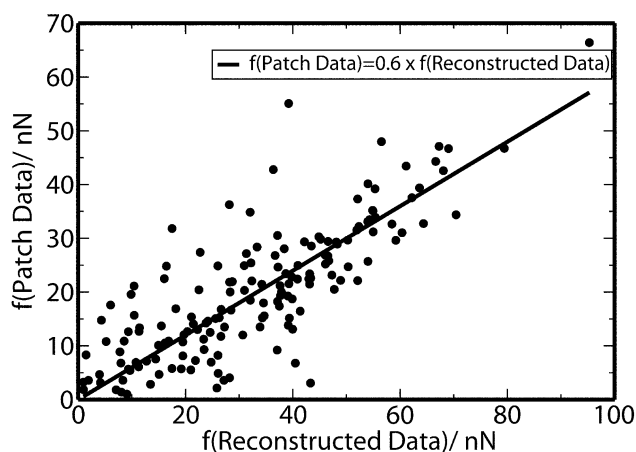


Fig. 6 Correlations between forces obtained from areas of overlap of reconstructed spheres and those from direct measurements of areas from the highlighted patches.

arising from both methods are strongly correlated, with an approximately linear relationship between the two. Moreover, we find that the form of the probability distribution $P(f)$ is not strongly dependent on α in the given range, and therefore assume the Princen model where $\alpha = 1$ throughout this study. In future work we plan to extract the dependency of the accurate force model on the coordination number by careful comparison of these data.

2.3 Experimental results

We have described the methodology used to calculate interdroplet forces in the previous section, and here we present the results of this analysis and a critical appraisal. Fig. 7 shows the probability distribution of interdroplet forces, $P(f)$, for the sample shown in Fig. 2(b). We use the Princen model (eqn. (3), $\sigma = 9.8 \times 10^{-3} \text{ N m}^{-1}$)²⁴) to obtain the interdroplet forces from the contact area data extracted from the image analysis described in Section 2.1. The forces are calculated from the bright, fluorescent patches that highlight the contact areas between droplets, because we believe they represent the areas of deformation arising from real forces within the system. The radii of the droplets needed to obtain the forces according to eqn. (3) are obtained with the Fourier Filtering Method. The distribution data shown are extracted from 1234 forces arising from 450 droplets. The data shows an exponential distribution at large forces, consistent with results of many previous experimental and simulation data on granular matter, foams, and glasses. The behaviour in the low force regime indicates a small peak, although the power law decay tending towards zero is not well pronounced.

The best fit to the data gives a functional form of the distribution $P(f) \propto f^{0.9} e^{-1.9f/\bar{f}}$, consistent with the theoretical model proposed in Section 3 and the existing literature.¹¹ It is inappropriate to draw conclusions on the physical significance of these coefficients, since the geometry of the packing in the experiment is very different to our simple theoretical model.

The experimental data obtained from geometric considerations of reconstructed droplet overlaps (also using the centers of the droplets obtained *via* the Fourier Filtering Method) are extremely useful in examining the locations of the highlighted contacts by visualisation techniques and in inferring the deviations from the Princen model for the force in our complex, compact system. The reconstructed patches also exhibit a probability distribution of an exponential form above the mean force, but the fitting coefficients between the two methods are not in agreement. Since the reconstructed patches are not a true measure of the stress transmission through the system, we do not include this data.

Our experimental data allows us to examine the spatial distribution of the forces in the compressed emulsion, shown in Fig. 8. In this admittedly small sample volume, the forces appear to be uniformly distributed in space and do not show evidence of localisation of forces within the structure. Moreover, we find that the average stress is independent of direction, indicating isotropy. Other experiments are underway to probe the existence of force chains in compressed emulsion systems.

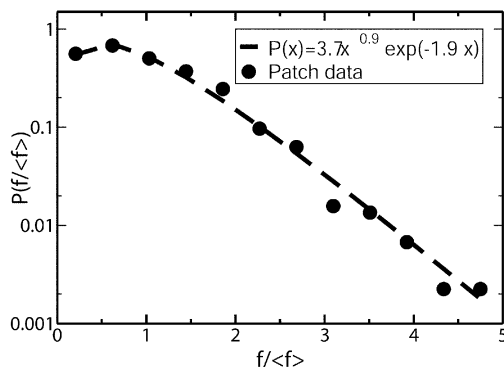


Fig. 7 Probability distribution of the contact forces for the compressed emulsion system shown in Fig. 2(b). We also show a fit to the theory developed in Section 3.

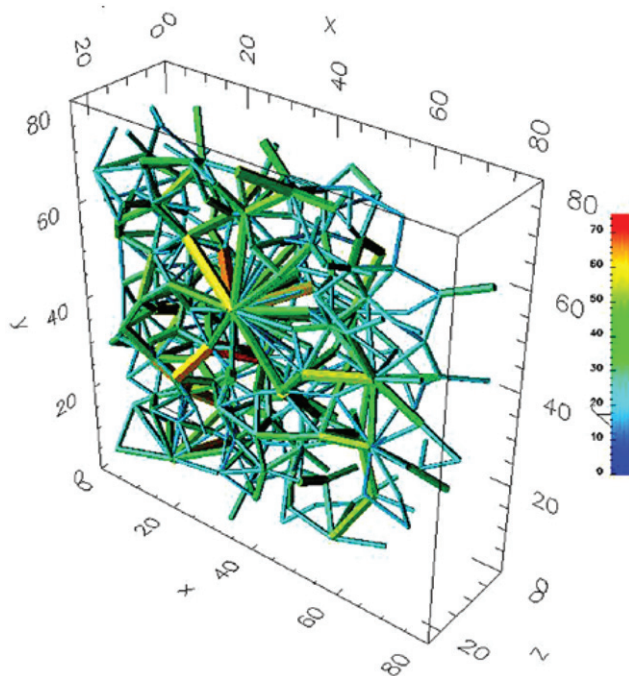


Fig. 8 Plot of the interdroplet forces inside the packing of droplets. We plot only the force larger than the average for better visualisation. Each rod joining the centers of two droplets in contact represents a force. The thickness and the colour of the rod is proportional to the magnitude of the force, as obtained from the area of contact using eqn. (3).

3 Theory

Although the experimental system consists of polydisperse particles which are deformable, in order to get a tractable theory, we simply consider spheres in multiple contact greater than or equal to three in 2D or four in 3D. Even though this is a gross simplification we believe that a theory that can be carried through to an analytic solution is worthwhile. The reader is referred to more comprehensive theories such as the q-model¹¹ or force-splitting models¹⁷ for more detailed analysis, which are correspondingly more difficult to solve.

3.1 The simplest model

By Newton's laws, in equilibrium the sum of all the forces exerted on a particle by its nearest neighbours is zero. In two dimensions the average shape of a particle is a circular disc, and the coordination number N of random close packing is three.³² Consequently the force \vec{f} exerted by a particle on one of its neighbours will equal the sum of the forces $\vec{f}_1 + \vec{f}_2$ of the other neighbours in contact with it. To simplify we consider the scalar $f = |\vec{f}|$ since it will have a very similar distribution on every grain. The distribution of the vector f will differ even on adjacent grains, therefore we calculate $P(f)$, not $P(\vec{f})$. It is important to note that only those forces which are pushing on each particle are taken into account in the calculation of $P(f)$, a fact which will appear in the range of integration. We look at first for the simplest possible model. The average force f_1 in the direction of f is $\frac{1}{2}|f_1|$ and similarly for f_2 . We now have

$$f = \frac{1}{2}f_1 + \frac{1}{2}f_2. \quad (4)$$

This gives rise to an equation of Boltzmann form

$$P(f) = \int_0^\infty \int_0^\infty df_1 df_2 \delta\left(f - \frac{1}{2}f_1 - \frac{1}{2}f_2\right) P(f_1)P(f_2). \quad (5)$$

It is convenient to work with the Fourier transform of the probability distribution $\mathcal{P}(k) = \int_{-\infty}^\infty e^{ikf} P(f)df$ which gives

$$\mathcal{P}(k) = \mathcal{P}^2(k/2). \quad (6)$$

The integral of the probability distribution is normalised to unity and so $\mathcal{P}(0) = 1$. The general solution of the above equation is $e^{i\bar{f}k - \beta|k|}$ giving a probability distribution

$$P(f) = \frac{\gamma\beta}{(f - \bar{f})^2 + \beta^2}, \quad (7)$$

where γ is a constant of integration. The contribution to $P(f)$ for $f < 0$ vanishes. This leads to $\beta = 0$ as the only possible solution, and we reach the rather obvious solution $P(f) = \delta(f - \bar{f})$.

A more accurate model would take into account the direction cosines of each of the forces. By taking the ‘‘averaged’’ particle to be a circular disc, we have implicitly assumed the forces are normal to it. Excluded volume is also an important factor as particles 1 and 2 cannot overlap and the four particle force correlation function should be included. All these effects can be crudely modelled by blurring the contribution from each of the pushing forces so that $\frac{1}{2}f_1$ is replaced by λf_1 where λ , which plays the role of the direction cosine and the other correlation factors, lies in the range 0 to 1. The ‘‘Boltzmann’’ equation now becomes

$$P(f) = \int_0^\infty \int_0^\infty df_1 df_2 \int_0^1 \int_0^1 d\lambda d\mu \delta(f - \lambda f_1 - \mu f_2) P(f_1)P(f_2). \quad (8)$$

Proceeding as before

$$\mathcal{P}(k) = \left(\int_0^1 d\lambda \mathcal{P}(\lambda k) \right)^2, \quad (9)$$

having the solution

$$P(f) = \frac{f}{p^2} e^{-f/p}, \quad (10)$$

which has been normalised and $p = \bar{f}/2$, where \bar{f} corresponds to the mean force. Note that since f is the sum of positive terms, whose value starts at zero, the distribution $P(f)$ must be zero at $f = 0$.

3.2 The 3D model

In 3D the co-ordination number of random close packing is greater than or equal to four.³² In this case the angular effects can be represented by three ‘‘direction cosines’’ λ_i and we find a force balance equation which is capable of analytic solution to be

$$f = \lambda_1^2 f_1 + \lambda_2^2 f_2 + \lambda_3^2 f_3. \quad (11)$$

Averaging the resulting force over the angles $\int_0^1 \lambda^2 d\lambda = \frac{1}{3}$ gives $f = \frac{1}{3}(f_1 + f_2 + f_3)$ representing equal weighting to each of the contact forces. Proceeding as before the Fourier transform of the probability distribution satisfies

$$\mathcal{P}(k) = \left(\int_0^1 d\lambda \mathcal{P}(\lambda^2 k) \right)^3, \quad (12)$$

which can be solved to give the normalised distribution

$$P(f) = \frac{2}{\sqrt{\pi}} \frac{f^{1/2}}{p^{3/2}} e^{-f/p}, \quad (13)$$

where $p \propto \bar{f}$ and the proportionality constant depends on the exponent of the power law rise at low forces. More generally, if there are N contacts arising from differing geometric configurations, similar calculations give

$$P(f) \propto f^{1/(N-2)} e^{-f/p}. \quad (14)$$

Note that for a large number of contacts, $P(f)$ reaches zero very near $f = 0$. There are many improvements which are essential for belief in coefficients, but the functional form, starting at zero and ending with an exponential decay, seems well founded.

4 Simulations

We perform numerical simulations (Molecular Dynamics, MD) to gain insight into the effects of osmotic pressure, polydispersity, and other microstructural features such as the coordination number and force chains on the probability distribution, $P(f)$. The system under investigation is an assembly of droplets. The numerical protocol is designed to mimic the experimental procedure used to prepare compressed emulsion systems at different osmotic pressures, described in Section 2. Our model considers an assembly of deformable spherical particles interacting *via* repulsive normal forces given by the Princen model in eqn. (3). For small deformations, the contact force is proportional to the overlap between the spheres in contact, defined as $\xi = (R_1 + R_2) - |\vec{x}_1 - \vec{x}_2|$, where \vec{x}_1 and \vec{x}_2 are the coordinates of the sphere centres. This linear relationship gives rise to a harmonic spring interaction between the droplets, $f \sim \xi$, with a spring constant given by the interfacial tension σ . However, since the force vanishes when $\xi < 0$, the interaction force must be highly nonlinear. More detailed analysis²⁹ have shown that the interdroplet forces can be represented by a nonlinear spring $f \sim \xi^\alpha$; the exponent α being dependent on the number of contact forces acting on the droplet. In this first study we only consider the Princen model in our simulations. More elaborate interparticle potentials will be considered in future investigations.

The continuous liquid phase is modeled in its simplest form, as a viscous drag force acting on every droplet, proportional to its velocity. The dynamical evolution of the droplets is obtained by solving Newton's equation for an assembly constrained by a given osmotic pressure. Our model is similar to the Discrete Element Method (DEM)^{8,33} often used in MD simulations of granular materials. However, we adjust the DEM for the system of compressed emulsions by exclusion of transversal forces (tangential elasticity and Coulomb friction) and by computation of interparticle forces using the Princen model instead of the Hertz model, often used in contact mechanics of solid particles ($f \sim \xi^{3/2}$).

The simulations begin with a set of non-overlapping 2000 spherical particles located at random positions in a periodically repeated cubic cell of side L . Generating a mechanically stable packing is not an easy task as shown by our previous computations.⁸ At the outset, a series of strain-controlled isotropic compressions and expansions are applied until a volume fraction slightly below the critical density of jamming is reached. The system is then compressed and extended slowly until a specified value of the stress and volume fraction is achieved at static equilibrium. The distribution of forces within the static structure is calculated and then directly compared to that obtained from experiments and theory.

We first consider a quasi-monodisperse system composed of 1000 droplets of radius 1.05 μm and 1000 droplets of radius 0.95 μm . Then the effect of polydispersity is investigated by consideration of the radii distribution obtained from our experiments (Fig. 1) characterized by a Gaussian distribution with a mean value of the $\langle R \rangle = 3.4 \mu\text{m}$ and standard deviation 1.44 μm , and a distribution range between 1 μm and 6.6 μm . The osmotic pressure, Π , is varied between 1 Pa and 1 kPa, again mimicking the experiments.

4.1 Simulation results

Fig. 9 shows the results of the simulations. The simulated data for monodisperse and polydisperse systems at low osmotic pressure agrees very well with the experiments and the theory. At low pressures the system is close to jamming (near RCP at $\phi \sim 0.64$) and the average coordination number is close to its minimal value $\langle N \rangle = 6$ for particles interacting by normal forces only as given by simple constraint arguments.^{8,32} At large pressures, when the coordination number significantly

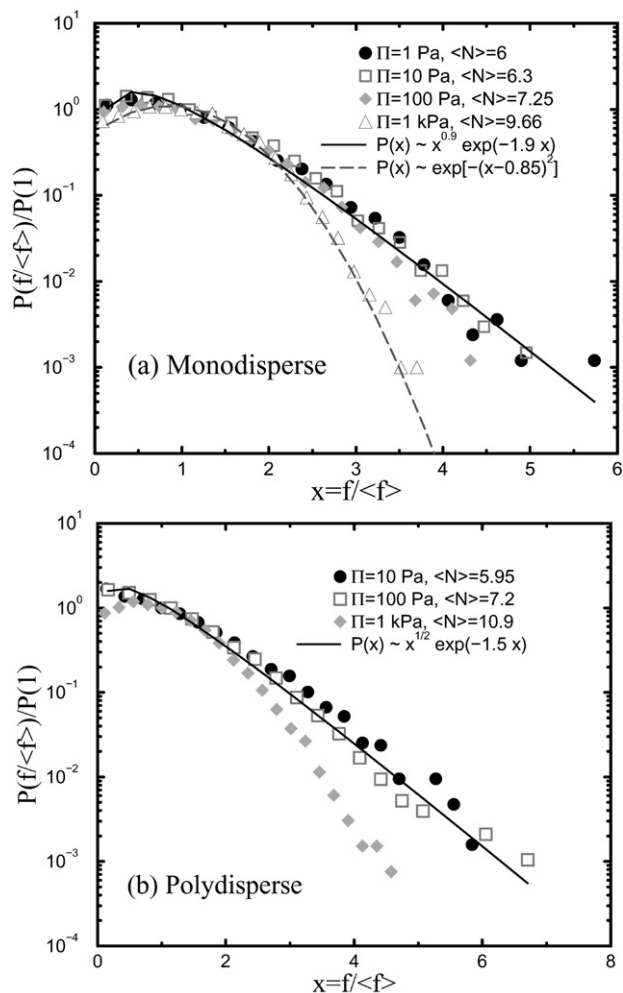


Fig. 9 Numerical results for $P(f)$ for a system of (a) monodisperse and (b) polydisperse emulsions at different osmotic pressure, Π , and mean coordination number $\langle N \rangle$.

departs from its minimal value, the probability distribution departs from the prediction of the theory and crosses over to a Gaussian-like distribution in the case of the monodisperse system. In the case of the polydisperse system, the distribution at large pressures departs from the exponential decay at large forces, but its form cannot be fitted by a Gaussian-like distribution.

The numerical simulation performed under the same conditions as in the experiment yields a $P(f)$ of the same functional form for the appropriate osmotic pressure ($\Pi \sim 100$ Pa) and polydispersity (Fig. 9b). Moreover, the monodisperse system shows similar results as long as the system is at low osmotic pressure. Our results indicate that the significant feature is not the detail of the system, but its proximity to the jamming transition.

5 Discussion and conclusions

We have presented experimental data showing the force distribution in three dimensions of a lightly compressed emulsion, close to the jamming transition. These data show an exponential distribution of interdroplet forces $P(f)$ at large f . At low f , a peak in the distribution function is observed. We have fitted the experimental data with a function of the form $P(f) \propto f^{0.9} e^{-1.9/f}$, suggested by the

simple theoretical model proposed for such a system. In addition we have carried out simulations to determine the effect of polydispersity and osmotic pressure on the force distribution function and these results are in very good agreement with the experimental data. They indicate that the $P(f)$ is not sensitive to polydispersity, however the exponential decay only fits the data well in distributions close to ‘jamming’, at low confining pressures. The theoretical model predicts a general distribution of the form $P(f) \propto f^n e^{-(n+1)f/f}$, where the power law coefficient n is determined by the packing geometry of the system. It is too crude a model to account for the complexity of the emulsion system, and it is therefore inappropriate to draw conclusions from direct comparisons of the coefficients obtained from theory with those arising from experimental and simulation data. Nevertheless, the agreement in the functional form for all three methods is an important result. Curiously, we observe that the fitting coefficients agree for the experimental data, the 2D theoretical model and the quasi-monodisperse emulsion system at a comparable pressure to the experiment.

In the future we hope to determine the mechanism by which the contact patches between droplets exhibit enhanced fluorescence and also to use the experimental data to test the validity of various force models for compressible droplets. In the experimental section we used the Princen model to obtain the interdroplet force from the contact area between particles. However in principle, we should be able to extract the force law from the data. This study gives supporting evidence to the universality of the concept of jamming and provides a very reliable experimental way of investigating microstructural elements within the bulk of any refractive index matched, closely packed system of an appropriate size.

Acknowledgements

We thank Jerome Bibette, Mark Shattuck, Andrew Tolley, John Melrose, Rafi Blumenfeld, Pietro Cicuta, and Beth Bromley for inspirational discussions. We are grateful to the EPSRC and the Petroleum Research Fund for support of this work.

References

- 1 *Jamming and Rheology: Constrained Dynamics on Microscopic Scales*, ed. A. Liu and S. R. Nagel, Taylor & Francis, London, 2001.
- 2 V. Trappe, V. Prasad, L. Cipelletti, P. N. Segre and D. A. Weitz, *Nature*, 2001, **411**, 772.
- 3 M. E. Cates, J. P. Wittmer, J.-P. Bouchaud and P. Claudin, *Chaos*, 1999, **9**, 511.
- 4 P. Dantu, *Géotechnique*, 1968, **18**, 50.
- 5 C. H. Liu, S. R. Nagel, D. A. Schechter, S. N. Coppersmith, S. Majumdar, O. Narayan and T. A. Witten, *Science*, 1995, **269**, 513.
- 6 F. Radjai, M. Jean, J. Moreau and S. Roux, *Phys. Rev. Lett.*, 1996, **77**, 274.
- 7 C. Thorton, *KONA Powder Part.*, 1997, **15**, 81.
- 8 H. A. Makse, D. L. Johnson and L. M. Schwartz, *Phys. Rev. Lett.*, 2000, **84**, 4160.
- 9 S. J. Antony, *Phys. Rev. E*, 2001, **63**, 11 302.
- 10 C. S. O’Hern, S. A. Langer, A. J. Liu and S. R. Nagel, *Phys. Rev. Lett.*, 2001, **86**, 111.
- 11 S. N. Coppersmith, C.-H. Liu, S. Majumdar, O. Narayan and T. A. Witten, *Phys. Rev. E*, 1995, **53**, 4673.
- 12 D. M. Mueth, H. M. Jaeger and S. R. Nagel, *Phys. Rev. E*, 1998, **57**, 3164.
- 13 G. Lovoll, K. N. Maloy and E. G. Flekkoy, *Phys. Rev. E*, 1999, **57**, 5872.
- 14 D. L. Blair, N. W. Mueggenburg, A. H. Marshall, H. M. Jaeger and S. R. Nagel, *Phys. Rev. E*, 2001, **63**, 41 304.
- 15 M. G. Sexton, J. E. S. Socolar and D. G. Schaeffer, *Phys. Rev. E*, 1999, **60**, 1999.
- 16 H. M. Princen, *J. Colloid Interface Sci.*, 1983, **91**, 160.
- 17 J.-P. Bouchaud, P. Claudin, D. Levine and M. Otto, *Eur. J. Phys. E*, 2001, **4**, 451.
- 18 U. Gasser, E. R. Weeks, A. Schofield and D. A. Weitz, *Science*, 2001, **292**, 258.
- 19 A. van Blaaderen and P. Wiltzius, *Science*, 1995, **270**, 1177.
- 20 E. R. Weeks, J. C. Crocker, A. C. Levitt, A. Schofield and D. A. Weitz, *Science*, 2000, **287**, 627.
- 21 I. I. Smalyukh, S. V. Shiyonovskii and O. D. Lavrentovich, *Chem. Phys. Lett.*, 2001, **88**, 336.
- 22 E. H. C. Bromley and I. Hopkinson, *J. Colloid Interface Sci.*, 2002, **75**, 245.
- 23 H. Jinnai, T. Koga, Y. Nishikawa, T. Hashimoto and S. T. Hyde, *Phys. Rev. Lett.*, 1997, **78**, 2248.
- 24 T. G. Mason, J. Bibette and D. A. Weitz, *Phys. Rev. Lett.*, 1999, **75**, 2051.
- 25 T. G. Mason and J. Bibette, *Langmuir*, 1997, **13**, 4600.
- 26 J. R. Parker, in *Algorithms for Image Processing and Computer Vision*, Wiley, New York, Chichester, 1997.
- 27 E. C. Rericha, C. Bizon, M. D. Shattuck and H. L. Swinney, *Phys. Rev. Lett.*, 2002, **88**, 14 302.

- 28 N. F. Law and R. Chung, *Pattern Recognit.*, 2001, **34**, 2133.
- 29 M-D. Lacasse, G. S. Grest, D. Levine, T. G. Mason and D. A. Weitz, *Phys. Rev. Lett.*, 1996, **76**, 3448.
- 30 D. J. Durian, *Phys. Rev. E*, 1997, **55**, 1739.
- 31 D. C. Morse and T. A. Witten, *Europhys. Lett.*, 1993, **22**, 549.
- 32 (a) C. F. Moukarzel, *Phys. Rev. Lett.*, 1998, **81**, 1634; (b) S. F. Edwards and D. V. Grinev, *Phys. Rev. Lett.*, 1999, **82**, 5397.
- 33 P. A. Cundall and O. D. L. Strack, *Géotechnique*, 1979, **29**, 47.